ETH Zurich
Dept. of Information Technology and
Electrical Engineering

Paul Scherrer Institute (PSI)
Research Institute for Natural and
Engineering Sciences

X-ray Tomography Group
TOMCAT

Semester Thesis
Master of Science in Biomedical
Engineering

Wavelet-based regularizers for iterative tomographic reconstruction in Grating Interferometry Breast CT

Semester Thesis

Submitted to
X-ray Tomography Group
Dept. of Information Technology and Electrical Engineering
ETH Zurich

Towards
MASTER OF SCIENCE IN BIOMEDICAL ENGINEERING

By
Sandra Haltmeier

Prof. Dr. Marco Stampanoni	Supervisor
Prof. Dr. Rima Alaifari	Supervisor
Dr. Michal Rawlik	Advisor
Stefano van Gogh	Advisor
Dr. Jinqiu Xu	Advisor

June 2022

Abstract

Breast cancer is the most common cancer in women causing more than half a million deaths a year. While breast cancer screening programs reduce mortality significantly, they come with the unpleasant side effects of painful examinations and high false positive rates. Grating interferometry breast computed tomography (GI-BCT) has the potential to revolutionize breast cancer imaging by offering increased patient comfort and superior image quality compared to routinely available imaging techniques. In GI-BCT three signals (absorption, phase and dark-field) can be obtained, whereof phase is the one of main interest, since it has the potential to outperform conventional attenuation contrast at high resolutions. However, the noise nature of the phase signal is challenging, especially at low visibility which is currently the case in GI-BCT. To solve the difficult inverse problem, we implemented an iterative phase reconstruction algorithm called fast composite splitting algorithm (FCSA) that combines wavelet-based sparsity promotion and total variation (TV) in the regularization term. FCSA achieved good image quality for simulated and experimentally measured phase contrasts at high radiation dose. For lower dose, and therefore higher noise, the regularizer with its selected hyperparameters has not been sufficient to produce high image quality. Nonetheless, the implemented iterative reconstruction method with a wavelet-TV regularization is a valuable tool for phase reconstruction in GI-BCT.

Acknowledgments

I would like to thank my supervisor Stefano van Gogh for his support and guidance during my semester project. Also I want to thank Prof. Dr. Marco Stampanoni from the x-ray tomography group at ETH Zurich for making this project possible. Special thanks go to Prof. Dr. Rima Alaifari for supporting me in terms of wavelet transforms and wavelet-based regularization. Moreover, a huge thank you to Dr. Jinqiu Xu and Dr. Michal Rawlik for their code, which I could use as a starting point for the projection data simulations and algorithm implementations. Finally I would like to thank Alexandre Vieira Pereira for the provision and support with the experimental data of the mastectomy.

Sandra Haltmeier

Zurich, June 7, 2022

Contents

1 Introduction

Each year more than two million women are confronted with a breast cancer diagnosis [1]. An early detection is key for survival and even with extensive breast cancer screening programs, more than half a million women a year die due to this disease [1]. Mammography is the gold standard in breast cancer detection and, although it significantly reduces breast cancer mortality [2], it has severe limitations in terms of patient comfort. Moreover, its sensitivity (86.9%) and specificity (88.9%) leave room for improvement [3]. Additionally, poor soft-tissue contrast and the lack of 3D data acquisition make image interpretation in mammography difficult, which often leads to small tumors being missed [4]. In fact, one fourth of breast cancer tumors are detected later than stage 1 [3].

Phase contrast breast computed tomography (PC-BCT) could not only provide 3D images, but also has the potential to increase the soft-tissue contrast compared to absorption-based CT [5]. In phase contrast imaging the phase shifts of x-rays propagating through a sample are measured. The physical parameter responsible for matter interactions, such as phase shifts, is the complex refractive index n that can be written as follows:

$$n(r, E) = 1 - \delta(r, E) + i\beta(r, E) \tag{1}$$

with r being the position within the object and E the x-ray energy. β determines the x-ray attenuation, whereas δ determines the phase shift. The phase shift is material- and x-ray energy-dependent and can vary between $-\pi$ and π [6]. In the energy range of mammography x-rays, the δ values of breast tissue can be up to 1000 times higher than the corresponding β values [7]. This effect is even enhanced for higher energy ranges, since harder x-ray beams lead to lower attenuation while the phase shift remains strong [8]. For PC-BCT, higher energies are often preferred due to the reduced dose deposition in breast tissue.

There are many approaches for phase contrast imaging (PCI) [6, 9, 10, 11], one of them being grating interferometry (GI) [12]. The foremost advantage of GI is that it can be realized with conventional x-ray sources and does not depend on the high flux and strong coherence of synchrotron radiation [12]. In grating interferometry breast computed tomography (GI-BCT) a conventional x-ray source in combination with gratings of small pitch sizes are used to generate a partially coherent, alternately phase shifted x-ray beam. The emerging interference pattern will then be distorted when propagating through the sample. By measuring the distortion at multiple grating positions, three signals (absorption, phase and scattering) can then be retrieved and individually reconstructed [13, 14]. Although in the last years the retrieval and reconstruction of the phase signal has been the object of extensive research [15, 16, 17], the image quality still needs to be significantly improved in order for the technology to be applied in a clinical context. Limitations in grating fabrication [18] combined with the unique noise behaviour in phase signals [19] make high resolution phase reconstruction challenging.

While analytical phase reconstruction, such as filtered backprojection (FBP), yields good results for low-noise projection data, its image quality severely worsens for higher noise levels. Moreover, analytical reconstruction algorithms can not be applied for intensity-based iterative phase reconstruction, which will be needed in clinical applications since measuring multiple grating positions is time consuming and dose intensive [20]. On the other hand, intensity-based iterative reconstruction allows to simultaneously reconstruct the attenuation coefficient, the refractive index and the linear diffusion coefficient from a single measurement per projection angle, which is more efficient, both in terms of dose and measurement time. Moreover, it is compatible with continuous gantry movement. For image reconstruction an iterative algorithm is needed that minimizes a cost function depending on the three signal quantities [21].

Iterative reconstruction methods contain a data term that estimates the likelihood of the reconstructed image and a regularization term that favours a solution with a certain property, for example piecewise continuity or smoothness [21]. Two main regularization types have been used for reconstructing GI-BCT data so far. TV was not able to yield satisfactory results as it introduced a trade-off between contrast-to-noise ratio (CNR) and image sharpness [16, 20]. Conversely, machine learning-based regularization produced very good reconstruction results but is by its nature a black-box approach and may lack stability for ill-posed inverse problems.

A common regularization term in magnetic resonance imaging reconstruction favours a small l_1-norm in a wavelet domain [22, 23, 24]. These wavelet-based priors produce good results in regard of noise reduction, artifact suppression, edge sharpness and reconstruction speed [24]. Additionally, wavelet-based regularization has been mathematically analyzed in depth and the convergence has been proven for many iterative algorithms [25, 26]. Although this kind of regularization has been used for x-ray computed tomography reconstruction before, to our knowledge its performance on GI-BCT has not yet been investigated.

The aim of this project is to develop a handcrafted regularization term based on wavelet transforms which promotes signal sparsity and can be used for iterative phase image reconstruction. We aim for a high image quality with high CNR and sharp edges as well as for a fast reconstruction algorithm. In view of later clinical applications, we used iterative reconstruction methods to pave the way towards an intensity-based phase reconstruction with wavelet-based regularization.

2 Method

2.1 Grating Interferometry

To realize GI-BCT with a conventional x-ray source a special imaging setup is needed. In a Talbot interferometer three gratings are placed in the x-ray beam [27], i.e. G_0, G_1 and G_2 [12] as shown in Figure 1.

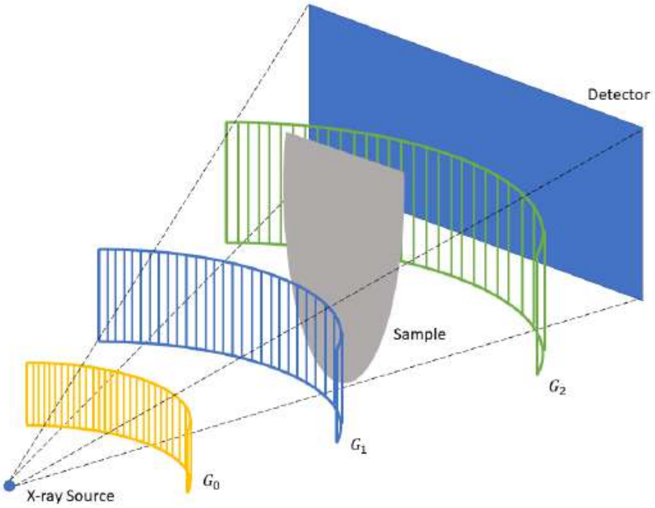

Figure 1: Schematics of GI-BCT with three gratings, G_0 (source grating), G_1 (beam-splitter grating) and G_2 (analyzer grating) with a cone-beam conventional x-ray source [20].

The source grating G_0 will increase beam coherence in one direction. The beam-splitter grating G_1, also called phase grating, generates an inference pattern by phase-shifting every second pitch by π [20]. The plane waves interfere and generate fringes at certain distances, called Talbot distances [28]. This inference pattern is then distorted when the beam passed through different materials. The tissue-induced phase shift becomes measurable with help of the analyzer grating G_2. The analyzer grating is an absorption grating and resolves the inference pattern such that each detector pixel will measure one intensity level based on the grating position [29].

2.1.1 Phase stepping and signal retrieval

To explicitly retrieve the three signals (attenuation, phase and scattering) in the projection domain, multiple inference patterns, and therefore multiple grating positions, must be measured. Which grating of the three is moved is not relevant, but for the signal retrieval to be successful, a minimum of three phase steps must be acquired [28]. Based on these measurements, a sinusoidal curve called phase stepping curve can then be fitted, as shown in Figure 2. When the fitted intensity curve of a flat field scan is compared to the curve of the object measurement, the three signals become separable. The attenuation coefficient μ is related to the difference in the average intensity. The refractive index δ

on the other hand can be calculated based on the phase difference φ of the sine curves. Finally, the linear diffusion coefficient ϵ is related to the ratio of the two amplitudes. Once the three signals are retrieved, they can be reconstructed individually.

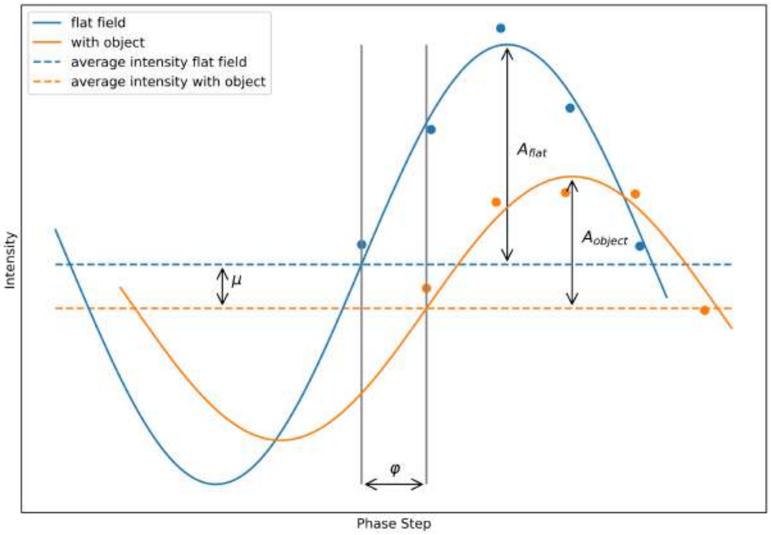

Figure 2: Sketch of a phase stepping curve for a flat field scan (blue) and for an object measurement (orange). The marked distances are used for signal retrieval. μ relates to attenuation, ϕ to phase shift and the ratio A_{object}/A_{flat} to scattering.

The phase stepping is time consuming and dose intensive. Yet, so far the best results in image quality have been achieved with this pre-reconstruction signal retrieval. However, for clinical applications it is probable that only grating interferometry with intensity-based reconstruction will be applicable, which means that the three signals will be disentangled during the reconstruction itself [20].

2.1.2 Phase signal and noise power spectrum

Let's call the phase shift of the phase stepping curve φ. The wavefront phase profile Φ is related to φ by

$$\varphi = \frac{\lambda d}{g_2} \frac{\partial \Phi}{\partial x} \tag{2}$$

with λ being the x-ray wave length, d the distance between G_1 and G_2 and g_2 the pitch size of the analyzer grating [30]. The refraction angle α of the x-ray beam is then given as follows:

$$\alpha = \frac{\lambda}{2\pi} \cdot \frac{\partial \Phi}{\partial x} \tag{3}$$

[31]. Finally, the refractive index δ is directly related to the refraction angle by the line integral of the first-order derivative as given by

$$\alpha = -\frac{\partial}{\partial x} \int_{-\infty}^{\infty} \delta \, dy \tag{4}$$

[18]. By combining the three equations above a relation between the refractive index and the measurable phase shift φ can be derived. It is given by

$$\varphi = C_\varphi \cdot \frac{\partial}{\partial x} \int_{-\infty}^{\infty} \delta \, dy = A\delta \tag{5}$$

with scaling parameter C_φ and differential projection operator A. Differential operators are much more complicated to build and difficult to use in a reconstruction task, wherefore phase reconstruction turns out to be significantly more difficult than absorption, which has a non-differential projection operator [32]. Additionally, the differential nature of the line integrals must be discretized in the projection operator. This can be done in several fashions. In this project the finite difference approximation was used, given by the following equation:

$$\varphi \approx C_\varphi \left(\int_y \delta dy - \int_{y+1} \delta dy \right) = (A_0 - A_1)\delta \tag{6}$$

with A_1 being the same matrix as A_0 but with each row shifted down by one, such that the derivative in the line integral is approximated with the difference in intensity of the line integrals of neighboring pixels [20]. Both matrices A_0 and A_1 consist of non-differential line integrals for multiple projection angles.

Not only the differential operator introduces complexity to the phase reconstruction problem, also the noise power spectrum of phase contrast does. While for attenuation the dominant noise is introduced in high frequencies, for phase it is located in the lower part of the frequency spectrum [19]. As a result, the quality of phase contrast compared with its attenuation counterpart is largely dependent on the image resolution. Phase image quality will surpass attenuation in high resolution images [19]. Yet, the resolution in general is limited by the required CNR and the tolerable level of dose, which makes if difficult for phase contrast to compete with attenuation in a clinical setting [20]. As shown in Figure 3, the noise in the differential phase sinograms seems much more intense compared to attenuation, especially in the low resolution areas of the simulated image. Yet, the high resolutions, such as edges, seem stronger.

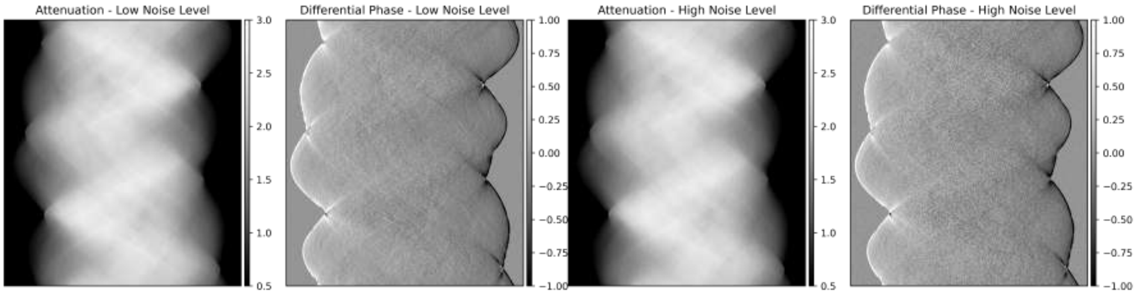

Figure 3: Attenuation and differential phase retrieved sinograms for a low noise level (3'000 photons per phase step, visibility 0.3) and a high noise level (1'000 photons per phase step, visibility 0.3).

2.2 Wavelet Transform

The wavelet transform is similar to a windowed Fourier transform performed at multiple scales [33]. One of its biggest advantages is that many natural signals have a sparse representation in the wavelet domain [34]. Due to noise and other signal artefacts, natural signals, especially in images, do often not represent physically meaningful quantities. For example, the ill-posed nature on many image reconstruction problems leads to poor image quality. Yet, in the wavelet domain we can better distinguish between the underlying physical signal and the overlaying noise. This fact is often used in image denoising and image reconstruction by enforcing wavelet-based sparsity and therefore select a physically meaningful solution. The basic ingredients of the wavelet transform are windowed waveform functions called wavelets [33].

2.2.1 Wavelets

Wavelets are formed by scaling and translating a basis function $\psi(t)$, the so called mother wavelet. This wavelike basis function has three important properties. Fist of all, contrary to a sine or cosine function, a wavelet is not only localized in the frequency but also in the time domain and therefore wavelets are often used for time and frequency analysis of a signal. Second, the total area under the curve is zero, which is essential for energy conservation in wavelet transforms. Finally, the function has a finite energy. A finite energy means that the integral of the absolute values squared is finite, which also implies that wavelets are of limited extent and have a start and end point [35]. A general 1D wavelet can be defined by the equation:

$$\psi_{a,b}(x) = \frac{1}{\sqrt{|a|}}\psi\left(\frac{x-b}{a}\right) \tag{7}$$

where a and b are real variables used to scale and translate the mother wavelet [35]. The scaling factor a determines the length of the wavelet which is often noted as a number next to the wavelet name. For example db4 is the shortcut for a Daubechies wavelet of length 4. Due to the normalization factor $a^{-1/2}$, the energy of the wavelet function remains independent of a. This property is important for energy conservation in multi-scale wavelet transforms where a changes its value [36].

Wavelets can be grouped into families that have mother wavelets with similar properties. Three exemplary mother wavelets of different families are illustrated in Figure 4. The Haar wavelet is often mentioned as the first and simplest wavelet. One of the most common wavelet families are the Daubechies wavelets, which are the first identified compactly supported, orthogonal wavelet basis of $L^2(\mathbb{R})$ [37]. Another orthogonal wavelet family is the Symmlet family. Orthogonal wavelets in general reduce the redundancy in the wavelet coefficients extracted via a wavelet transform [33]. Therefore, they are used in discrete wavelet transforms, where extracted coefficients are of limited extend and redundancy is unwanted. While all wavelet families have advantages and disadvantages for different applications, in wavelet-regularized image reconstruction the Daubechies wavelets established themselves as a standard [38, 39, 40]. Thus, we decided to use Daubechies wavelets in this work.

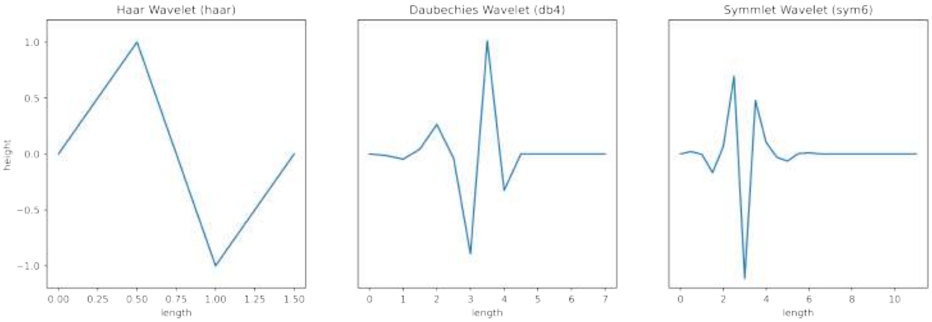

Figure 4: Three wavelet function examples of different families: Haar of length 1 (haar), Daubechies of length 4 (db4) and Symmlet of length 6 (sym6).

2.2.2 Discrete Wavelet Transform (DWT)

The discrete wavelet transform (DWT) transforms any given vector into a set of mutually orthogonal wavelet coefficients by using a discrete set of wavelet scales. Those coefficients can then be used for wavelet-based compression, denoising, regularization or coding [35]. The DWT in 1D splits the input signal into a detail (see Equation 8) and a trend signal (see Equation 9) as illustrated in Figure 5. The two element-wise wavelet coefficient vectors W_ψ (detail) and W_ϕ (trend) can be defined with the following equations:

$$W_\psi(j,k) = \frac{1}{\sqrt{M}}\sum_x f(x)\psi_{j,k}(x) \tag{8}$$

$$W_\phi(j,k) = \frac{1}{\sqrt{M}}\sum_x f(x)\phi_{j,k}(x) \tag{9}$$

where $f(x)$ is the discrete function which shall be transformed and M is the number of elements in the input. $\phi_{j,k}(x)$ is a translated (by k) and scaled (by j) version of a scaling function $\phi(x)$. $\psi_{j,k}(x)$ is a translated (by k) and scaled (by j) wavelet basis function. The function $f(x)$ can also be the trend coefficients from a previous wavelet transform. For scale j it must hold that $j \geq j_0$ with j_0 being the lowest scale, defined by the input data size and the wavelet length. If only one scale (j_0) is used, it is called a single-scale discrete wavelet transform, whereas for multiple scales j it is called multi-scale DWT [35].

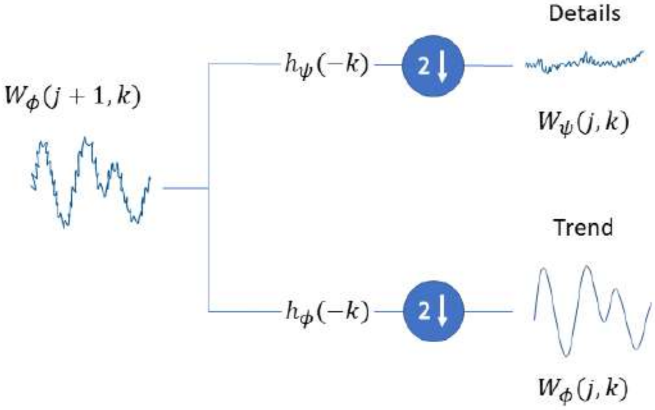

Figure 5: Schemata of 1D DWT: Left signal $W_\phi(j+1,k)$ is convolved with a high pass filter h_ψ and down-sampled by 2 to get detail coefficients $W_\psi(j,k)$. The similar procedure with a low pass filter h_ϕ leads to the trend signal $W_\phi(j,k)$, which can be used as input signal for the next wavelet transform scale.

The DWT can not only be seen as a sum over a multiplication with a wavelet function (Equation 8), but also as a convolution with a wavelet-dependent high pass filter h_ψ and a down-sampling by two. Similarly, the trend coefficients (Equation 9) can be calculated by a convolution with a wavelet-dependent low pass filter h_ϕ followed by a factor two down-sampling.

Multi-Scale Discrete Wavelet Transform

In a multi-scale DWT a subsequent wavelet transform is performed on the trend signal of the previous step. Accordingly, instead of explicit equations, implicit equations can be established, as Equation 10 and Equation 11 show. Wavelet-dependent low pass (h_ϕ) and high pass filter kernels (h_ψ) are convolved with the trend signal of the previous iteration and then sub-sampled by a factor of two. For the initial iteration step with j equals the maximal scaling depth, W_ϕ is given by the input data, which is similar to a single-scale DWT [35].

$$W_\psi(j,k) = h_\psi(-2k) * W_\phi(j+1,2k) \tag{10}$$
$$W_\phi(j,k) = h_\phi(-2k) * W_\phi(j+1,2k) \tag{11}$$

Given that the lower the scaling factor j the more sub-sampled the input signal is, j controls coarseness of the signal details described by the wavelet coefficients. In other words, the lower the scale j, the lower the transformed frequency captured in the scale-specific wavelet coefficients [33].

Two Dimensional Discrete Wavelet Transform (2D-DWT)

The 2D-DWT generalizes the 1D-DWT. Due to the DWT's property of being separable, two single transforms can be performed individually for the rows and columns of the input data. Figure 6 illustrates a wavelet transform decomposition tree at a single scale for a 2D input image.

The detail coefficients are extracted by applying a wavelet function ψ to the input image's rows, columns or both subsequently. This results in three detail coefficient arrays often referred to as horizontal (rows), vertical (columns) and diagonal (rows and columns) details. Equation 12 displays the performed wavelet transforms to extract those detail coefficients. The trend image is calculated via Equation 13 and results from a row- and column-wise input scaling [33].

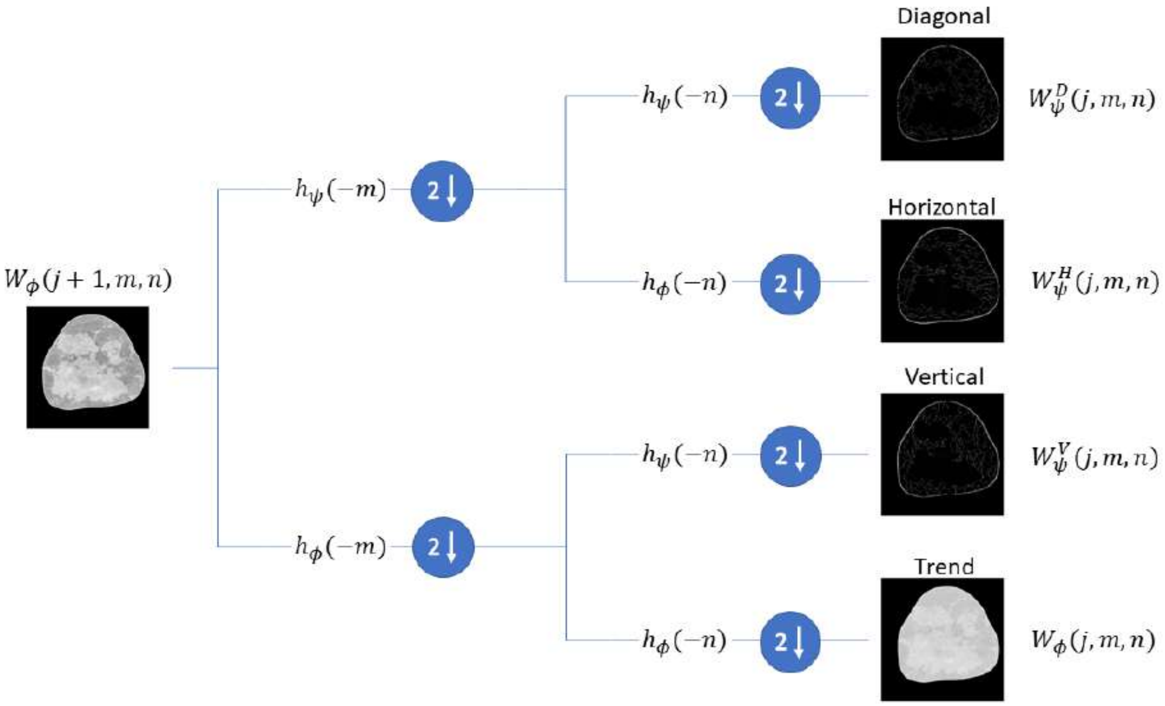

Figure 6: Schemata of 2D-DWT: Convolution and down-sampling of the left signal with high (h_ψ) and low (h_ϕ) pass filter kernels for rows (m) and columns (n) leads to diagonal, horizontal and vertical detail coefficients as well as the trend signal. The trend signal to the right can then be used as input for the next wavelet transform scale.

$$W_\psi^{D,H,V}(j,m,n) = \frac{1}{\sqrt{MN}} \sum_{x=0}^{M-1} \sum_{y=0}^{N-1} f(x,y)\psi_{j,m,n}^{D,H,V}(x,y) \tag{12}$$

$$W_\phi(j,m,n) = \frac{1}{\sqrt{MN}} \sum_{x=0}^{M-1} \sum_{y=0}^{N-1} f(x,y)\phi_{j,m,n}(x,y) \tag{13}$$

The input $f(x,y)$ is of size $M \times N$. $\phi_{j,m,n}(x,y)$ is a scaled and translated version of the basis scaling function $\phi(x,y)$, which can be separated into $\phi(x,y) = \phi(x)\phi(y)$. The directional wavelet functions for rows, columns or rows and columns are given by $\psi_{j,m,n}^{D,H,V}$. The functions are composed of the basis wavelet function ψ applied to the direction of interest (row, column or both) and the basis scaling function ϕ, which suppresses any coefficients arising from the unwanted direction (column, row, none). As example for the horizontal details this means that per row (x) wavelet coefficients are extracted and per column (y) scaling is applied. The equations below show the composition of the directional wavelet functions for horizontal, vertical and diagonal details [35].

$$\psi^H(x,y) = \psi(x)\phi(y) \tag{14}$$

$$\psi^V(x,y) = \phi(x)\psi(y) \tag{15}$$

$$\psi^D(x,y) = \psi(x)\psi(y) \tag{16}$$

The 2D-DWT can also be expanded to multi-scale transforms by applying a subsequent transform on the trend image of the previous step. Moreover, the same principle can be derived for any dimension. It is important to note that the number of detail and trend coefficients arrays increases with the dimension d according to 2^d. For 2D it corresponds to 2^2 arrays named trend, diagonal, horizontal and vertical details [33].

Inverse Discrete Wavelet Transform (IDWT)

Similar to the Fourier transform an inverse wavelet transform (IDWT) can be defined as follows:

$$f(x,y) = \frac{1}{\sqrt{MN}} \sum_m \sum_n W_\phi(j_0,m,n)\phi_{j_0,m,n}(x,y) + \frac{1}{\sqrt{MN}} \sum_{i=H,V,D} \sum_{j=j_0}^{\infty} \sum_m \sum_n W_\psi^i(j,m,n)\psi_{j,m,n}^i(x,y) \tag{17}$$

The trend data W_ϕ is only needed for the lowest scale j_0 since the trend data of a higher scale can be reconstructed by the trend and detail coefficients of the scale below [35].

The discrete wavelet transform will from now on be indicated by W, the corresponding inverse discrete wavelet transform by W^{-1} and the wavelet coefficients by c. In this project, the python library "pywavelets" has been used to implement the wavelet transform [41].

2.3 Iterative Shrinkage Thresholding Algorithm (ISTA)

To solve linear inverse problems with a solution that is assumed to be sparse with respect to an orthonormal basis, such as a wavelet domain, the iterative shrinkage thresholding algorithm (ISTA) was developed [25]. The inverse problem in the context of differential phase computed tomography can be formulated in the following manner:

$$\underset{x}{\operatorname{argmin}} \, ||Ax - b||_2^2 + \lambda ||Wx||_1 \tag{18}$$

with A being the projection matrix, b the retrieved differential phase contrast sinogram, x the reconstructed image and W the DWT. The wavelet coefficients $c = Wx$ can then be transformed to the image x via the inverse wavelet transform $x = W^{-1}c$. ISTA solves a convex inverse problem in an iterative manner by using a gradient-based update step combined with a l_1-norm regularization [26], as Algorithm 1 explains in more detail.

Algorithm 1 ISTA

```
Input: initial guess $x^0 = 0$, retrieved differential phase contrast sinogram b, projection operator A,
    number of iterations K, DWT parameters (scale, wavelet, thresholds $\mu$)
Output: $x^K$
function ISTA($x^0, b, A, K, scale, wavelet, \mu$)
    calculate Lipschitz constant $L = 2\sigma^{max}(A^T A)$
    for k=0:K do
        Step 1
        gradient-based update
        $g^k = x^k + \frac{2}{L} A^T \cdot (b - Ax^k)$
        Step 2
        sparsity constraint in wavelet domain via soft-thresholding
        $x^{(k+1)} = S_{W,\mu}(g^k)$
    end for
    return $x^K$
end function
```

As regularization $S_{w,\mu}(g) = W^T \Gamma_\mu(Wg)$, the algorithm makes use of soft-thresholding to enforce sparsity in the wavelet domain. The soft-thresholding function Γ_μ shrinks all coefficients with absolute values below the threshold μ to zero, while reducing all other coefficients by the amount of the threshold. Soft-thresholding corresponds to the proximity operator of the l_1-norm. More precisely, it is equal to $\mu||g||_1$ with g being the input and μ the threshold [42]. The thresholding step is described by Equation 19 [43]. For multi-scale wavelet transforms, the soft-thresholding is performed on each scale individually. Consequently, the thresholds μ can vary between scales.

$$\Gamma_\mu(g) = \begin{cases} g + \mu & \text{if } g \leq -\mu \\ 0 & \text{if } -\mu < g < \mu \\ g - \mu & \text{if } g \geq \mu \end{cases} \tag{19}$$

The Lipschitz constant L is defined as two times the largest eigenvalue of $A^T A$ and applied as step size indication. The largest eigenvalue of a matrix can be estimated via the power method [44]. The Lipschitz constant depends on the projection matrix A and is therefore geometry dependent, for example it is dependent on the number of detector pixels. However, L is not sample dependent, wherefore it needs to be calculated only once in advance of the data reconstruction, as long as the geometry remains unaltered.

2.4 Fast Iterative Shrinkage Thresholding Algorithm (FISTA)

Although ISTA is straightforward and can be used for a multitude of linear inverse problems, the algorithm converges rather slowly. To reduce the computational time and enable a faster convergence, the fast iterative shrinkage thresholding algorithm (FISTA) was exploited [26]. The decreased convergence time builds upon a momentum term that updates the iterative reconstruction at the end of each iteration, i.e.

$$y^{k+1} = x^{k+1} + \frac{t^k - 1}{t^{k+1}}(x^{k+1} - x^k) \tag{20}$$

where x is the soft-thresholded image iterate, y is the reconstructed image used for the gradient update in the next iteration, t is an iteration dependent step size variable and k is the iteration number. The step size variable t is defined by

$$t^{k+1} = \frac{1 + \sqrt{1 + 4t^{k^2}}}{2} \tag{21}$$

FISTA can be implemented as explained in Algorithm 2. Due to its faster convergence, in this work mainly FISTA and variations of FISTA were investigated.

Algorithm 2 FISTA

Input: initial guess $x^0 = y^0 = 0$, initial step size $t^0 = 1$, retrieved differential phase contrast sinogram b, projection operator A, number of iterations K, DWT parameters (scale, wavelet, thresholds μ)

Output: x^K

```
function FISTA($x^0, y^0, t^0, b, A, K, scale, wavelet, \mu$)
    calculate Lipschitz constant $L = 2\sigma^{max}(A^T A)$
    for k=0:K do
        Step 1
        gradient-based update
        $g^k = y^k + \frac{2}{L} A^T \cdot (b - Ay^k)$
        Step 2
        sparsity constraint in wavelet domain via soft-thresholding
        $x^{k+1} = S_{W,\mu}(g^k)$
        Step3
        calculate $y^{k+1}$ based on $x^k, x^{k+1}$
        $t^{k+1} = \frac{1+\sqrt{1+4t^{k^2}}}{2}$
        $y^{k+1} = x^{k+1} + \frac{t^k-1}{t^{k+1}}(x^{k+1} - x^k)$
    end for
    return $y^{K+1}$
end function
```

2.5 Fast Composite Splitting Algorithm (FCSA)

The fast composite splitting algorithm (FCSA) is an algorithm based on FISTA that combines wavelet and total variation (TV) regularization in a least square linear inverse problem, i.e.

$$\underset{x}{\operatorname{argmin}} \, ||Ax - b||_2^2 + \alpha |x|_{TV} + \beta ||Wx||_1 \tag{22}$$

where α and β are parameters to control the relative regularization strength [45]. TV is a l_1-norm based on directional derivatives that can be promoted in an iterative manner and is therefore often called l_1 estimation procedure [46]. The formula is given by

$$TV(u) = ||\nabla u||_{2,1} = \left|\left|\sqrt{|\nabla_x u|^2 + |\nabla_y u|^2}\right|\right|_1 \tag{23}$$

with ∇_x, ∇_y as gradients in x resp. y direction and $\nabla = [\nabla_x; \nabla_y]$ [47]. In this project, the iterative algorithm of Chambolle [48] was used for the TV regularization. The particular reconstruction algorithm used in this work is shown in Algorithm 3 and was developed by Huang et al. [45]. All project code can be found in the GitLab project "pcpy" of the x-ray tomography group (TOMCAT) located at ETH Zurich and the Paul Scherrer Institute (PSI).

Algorithm 3 FCSA

```
Input: initial guess $x^0 = y^0 = 0$, step size $t^0 = 1$, retrieved differential phase contrast sinogram b,
    projection operator A, number of iterations K, DWT parameters (scale, wavelet, thresholds $\mu_W$),
    TV parameters $\mu_{TV}$
Output: $x^K$
function FCSA($x^0, y^0, t^0, b, A, K, scale, wavelet, \mu_W, \mu_{TV}$)
    calculate Lipschitz constant $L = 2\sigma^{max}(A^T A)$
    for k=0:K do
        Step 1
        gradient-based update
        $g^k = y^k + \frac{2}{L} A^T \cdot (b - Ay^k)$
        Step 2
        sparsity constraint in wavelet domain via soft-threshold
        $x_W^{k+1} = S_{W,\mu_W}(g^k)$
        total variation denoising
        $x_{TV}^{k+1} = TV_{\mu_{TV}}(g^k)$
        calculate the average of TV and wavelet regularized images
        $x^{k+1} = \frac{x_W^{k+1} + x_{TV}^{k+1}}{2}$
        Step3
        calculate $y^{k+1}$ based on $x^k, x^{k+1}$
        $t^{k+1} = \frac{1+\sqrt{1+4{t^k}^2}}{2}$
        $y^{k+1} = x^{k+1} + \frac{t^k - 1}{t^{k+1}}(x^{k+1} - x^k)$
    end for
    return $y^{K+1}$
end function
```

3 Results

To evaluate the performance of FISTA and FCSA simulated and experimentally measured data was used, as shown in Figure 7. The results for both data types were then compared to an analytical and a TV-based iterative reconstruction. As analytical reconstruction a filtered backprojection (FBP) with a Hilbert filter was applied [49]. The TV regularized reconstruction was implemented as an alternating direction method of multipliers (ADMM) [50]. In the ADMM-TV algorithm the data-based update was conducted via a least-square estimator from the scipy toolbox [51]. The regularization term was handled by the Chambolle TV algorithm [48]. In iterative phase reconstruction, the reconstructed image initially develops the high frequencies, such as edges. Then the lower frequencies follow, evolving from the outer borders towards the image middle. Yet, TV is a rather aggressive regularizer, especially before the contrast reached a certain value. Thus, a number of iterations were carried out without regularization term in the beginning of the ADMM reconstruction to allow better contrast development.

Due to time reasons, the hyperparameters for all three iterative algorithms (ADMM-TV, FISTA, FCSA) were determined by manual grid search and literature review. The wavelet used for the wavelet transform was a Daubechies wavelet of length 4 (db4). It was selected as a standard wavelet for image reconstruction based on recommendations from the literature [38, 39, 40] and evaluated for length 4,

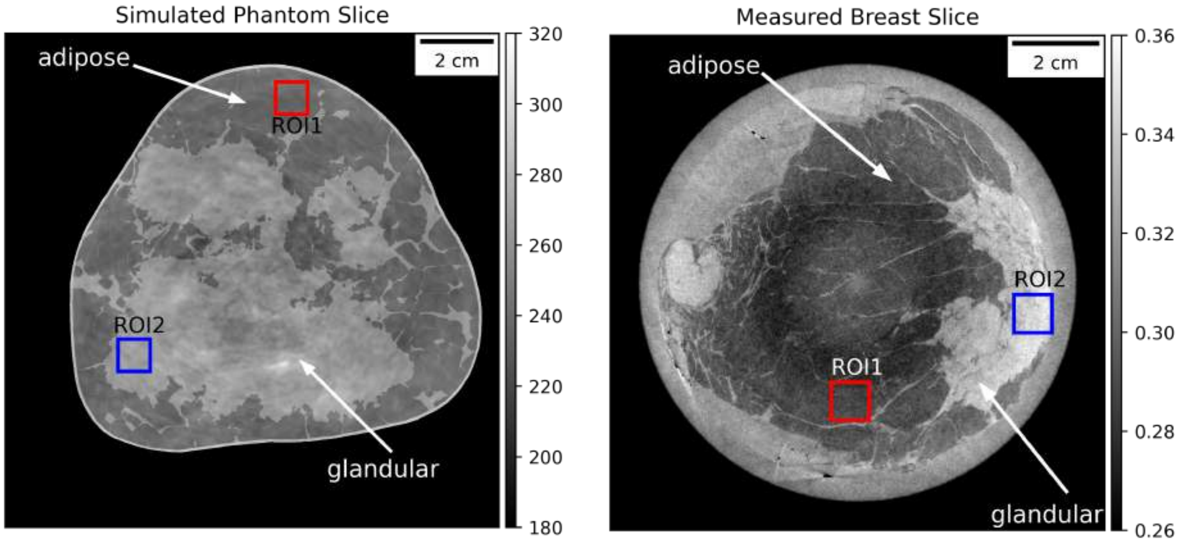

(a) (b)

Figure 7: Horizontal slice of (a) simulated phantom and (b) experimental measurements of a mastectomy. Two regions of interest (ROI) per data type were selected for quantitative evaluation of image quality.

6 and 8, whereof length 4 performed best in all cases. The wavelet regularizer of FISTA and FCSA was a three-scale wavelet transform with scale-dependent thresholds. The thresholds were set to be exponentially decreasing with decreasing scale. In other words, the threshold for the highest scale (fine scale) is highest and the threshold for the lowest scale (coarse scale) is closest to zero. Soft-thresholding was applied to the detail coefficients of all scales but not to the trend image.

For quantitative comparison of the reconstructed images, the contrast, the contrast-to-noise ratio (CNR) and the signal-to-noise ratio (SNR) were used. Owing to the available ground truth phantom of the simulation data, the image quality of this data could also be analyzed with the Mean Square Error (MSE) and the Structural Similarity (SSIM) metrics. The formulas are given as follows:

$$\text{Contrast} = 20\log_{10}\left(\frac{m_{ROI2}}{m_{ROI1}}\right) \tag{24}$$

$$CNR = \frac{|m_{ROI2} - m_{ROI1}|}{\sqrt{\sigma^2_{ROI2} + \sigma^2_{ROI1}}} \tag{25}$$

$$SNR = \frac{m_{ROI2}}{\sigma_{ROI1}} \tag{26}$$

$$MSE = \frac{1}{X \times Y \times Z}\sum_{x=1}^{X}\sum_{y=1}^{Y}\sum_{z=1}^{Z}(g_{x,y,z} - \overline{g}_{x,y,z})^2 \tag{27}$$

$$SSIM(g,\overline{g}) = \frac{(2m_g m_{\overline{g}} + C_1)(2\sigma_{g\overline{g}} + C_2)}{(m_g^2 + m_{\overline{g}}^2 + C_1)(\sigma_g^2 + \sigma_{\overline{g}}^2 + C_2)} \tag{28}$$

with m_{ROI} being the average and σ_{ROI} the standard deviation of the pixel intensity over a region of interest (ROI), g the reconstructed image and $\overline{g}$ the reference image [20]. The contrast unit is given in decibel (dB) and the constants C_1 and C_2 are used to prevent a zero denominator. The five metrics tend to be non-consistent among each other, since they focus on different aspects of image quality. If an image performs best in all five categories it should also score highest in visual quality inspection.

3.1 Convergence ISTA vs. FISTA

Initially, a convergence analysis was carried out to compare the convergence behaviour of ISTA and FISTA. As Figure 8 shows, FISTA has a much faster convergence (after 300 iterations for the simulation-based reconstruction volume of 1536 × 1536 × 16 and low noise level). ISTA also converges but only after 2500 iterations. Due to the major difference in convergence velocity and therefore in computation time, we used FISTA and its extension FCSA.

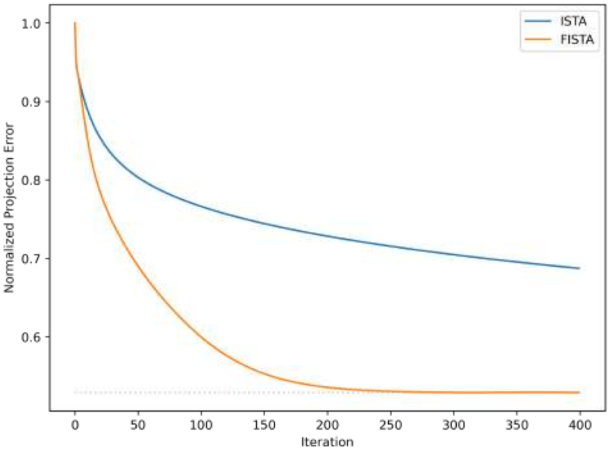

Figure 8: Convergence comparison of ISTA and FISTA for a simulation-based reconstruction volume of 1536 × 1536 × 16.

3.2 Reconstruction results for simulated data

For the simulated data a breast phantom was constructed based on an attenuation breast CT measured at the University Hospital Zurich under ethically approved patient informed consent [52, 53]. The simulated phantom, as illustrated in Figure 7a, was then used with a cone-beam x-ray forward operator implemented with the ASTRA toolbox [54] to generate the projection data. A phase stepping of five steps was used to simulate the phase stepping curve. The number of photons per phase step as well as the visibility could be adjusted to generate multiple noise levels. In this work two noise levels were evaluated. The low noise level was generated with a visibility of 0.3 and 3'000 photons per step. The high noise level corresponds to a visibility of 0.3 and 1'000 photons per step. To reduce computation time, only the 16 innermost slices of the breast phantom were reconstructed. The reconstruction geometry is listed in Table 1.

Table 1: Reconstruction geometry for simulated data.

Parameter	Value
Number of projections	600
Angular scanning interval	$2\pi/600$
Number of detector pixels	1536 × 16
Reconstructed image size	1536 × 1536 × 16
Sample-source distance	1.03 m
Sample-detector distance	0.74 m
Image voxel size	$87.29 \times 87.29 \times 87.29\ \mu m^3$

3.2.1 Low noise level

For the noise level at visibility 0.3 and 3'000 photons per phase step the best parameters found for FISTA were wavelet thresholds (0.002, 3, 100) for scale (1-coarse, 2, 3-fine) with 300 iterations. The image quality of FCSA was maximized by 300 iterations with the wavelet thresholds (0.005, 5, 100) and the TV weight parameter 0.01. FCSA's iterative TV was limited by the maximum iteration number of 40, i.e. for each gradient-based update a TV estimation with a maximum of 40 updates was performed. Finally, the ADMM-TV algorithm has been run with 40 initial iterations *without*, and another 80 iterations *with* regularization. The TV weight was set to 0.02 with a maximum iteration of 40.

Qualitative results

Figure 9 shows the qualitative results of the four reconstruction algorithms. All images are shown after the following normalization:

$$x_{i,j} = \frac{x_{i,j}}{\sum_{i,j}^{M,N} \frac{x_{i,j}}{g_{i,j}} \cdot \frac{1}{MN}} \tag{29}$$

with $x_{i,j}$ being the pixel intensity of the reconstructed image at location (i,j), $g_{i,j}$ the pixel intensity of the ground truth image at location (i,j) and $M \times N$ the image size. Due to the normalization, the color scales of the reconstructed images are comparable to each other and to the ground truth. The horizontal slice shown was taken from the middle of the breast phantom. The detail magnification is selected for comparison of image sharpness and small structure details.

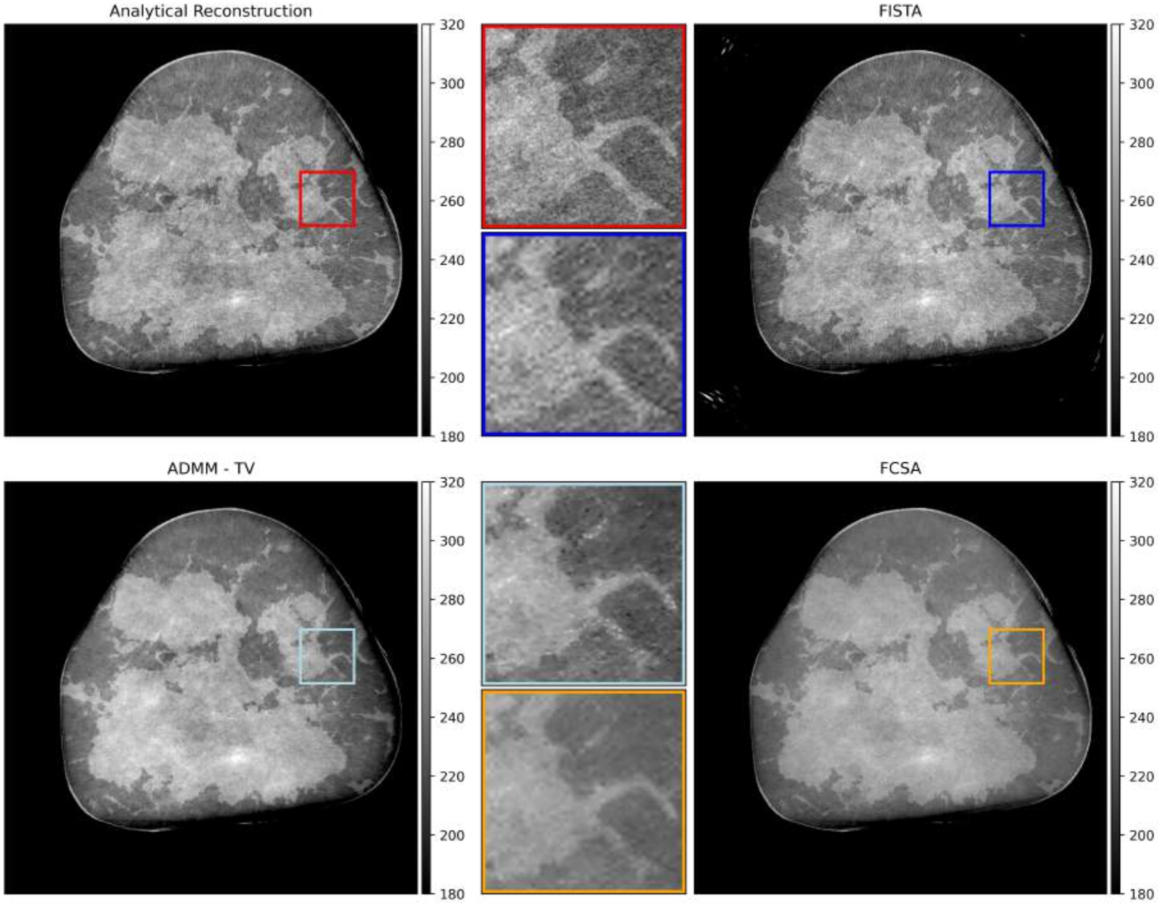

Figure 9: Reconstruction results for FBP with Hilbert filter, FISTA, TV regularization and FCSA for simulated data with low noise level (3'000 photons per phase step, visibility 0.3).

The FISTA reconstruction appears noisy, similarly noisy as the analytical reconstruction, and when looking at the magnification a pixelated structure can be observed. The edges are sharp but the image resolution seems decreased. For FSCA on the other hand, the image is very smooth and the noise is almost completely gone. Small structures are still detectable, however the contrast between the adipose and glandular tissue seems reduced. The edges are comparable sharp to the ones of the ADMM-TV reconstruction, yet not as sharp as the edges of the FBP.

Quantitative results

Because of the inhomogeneities inside the ROIs, the ground truth phantom has a maximum contrast between adipose and glandular tissue of 2.3737 dB and a corresponding CNR of 5.5476. The SNR is set at 63. The analytical solution performs best in terms of MSE with a value of 300.19. The TV regularized reconstruction has the highest contrast of 4.1389 dB and the best CNR with a value of 6.9066. Finally, the FCSA has the highest structural similarity with 0.5656 as well as the best SNR with 99.67. No image has a clear overall advantage in the quantitative metrics and the metrics are inconsistent among each other. All quantitative results are summarized in Table 2. The best result per statistical measure is colored in blue.

Table 2: Quantitative evaluation of phase reconstruction algorithms on simulation data in the low dose regime. The best result per metric is colored in blue.

	Phantom	Analytical	ADMM-TV	FISTA	FCSA
Contrast (dB)	2.3737	2.5575	4.1389	2.506	2.1867
CNR	5.5476	2.2554	6.9066	2.8893	5.8235
SNR	63.0	27.45	56.26	35.37	99.67
MSE	0.0	300.19	557.90	329.65	307.23
SSIM	1.0	0.5453	0.5523	0.5413	0.5656

3.2.2 High noise level

The evaluation of FISTA and FCSA has also been done on simulation data in a high dose regime. A visibility of 0.3 and 1’000 photons per phase step lead to high noise in the phase signal. The noise is mainly present as high frequencies, even though a few low frequency noise patterns can also be found. The resulting algorithm specific hyperparameters can be found in Table 3.

Table 3: Algorithm-dependent reconstruction parameters for simulated data in high noise regime.

	Number of iterations *without* regularizer	Number of iterations *with* regularizer	Wavelet thresholds for scale (1,2,3)	Wavelet	TV weight	TV max. iteration
FISTA	-	300	(0.005, 10, 1000)	db4	-	-
ADMM-TV	40	80	-	-	0.5	40
FCSA	-	300	(0.01, 10, 500)	db4	0.02	40

Qualitative results

The qualitative results of FISTA and FCSA compared to FBP with Hilbert filter and ADMM-TV are shown in Figure 10. The displayed images were normalized as explained in Equation 29.

The analytical reconstruction and the FISTA result are corrupted by a lot of noise. Their edges become unclear and small features get lost due to the high noise level. Additionally, the FISTA reconstruction is very pixelated. ADMM-TV and FCSA on the other hand remove most of the noise, FCSA even slightly better, and have smooth structures. Yet, some edges and details are not visible anymore due to the low contrast. In FCSA the contrast is even lower than in ADMM-TV and both algorithms fight against salt-and-pepper noise.

Quantitative results

In the high noise regime, the TV regularized reconstruction and the FCSA results are of similar quality. On one side the ADMM-TV solution is better in terms of contrast (3.7486 dB), CNR (6.4972) and SSIM (0.5396). On the other side FCSA has an advantage in terms of SNR (82.79) and MSE (306.40). All statistical values are summarized in Table 4.

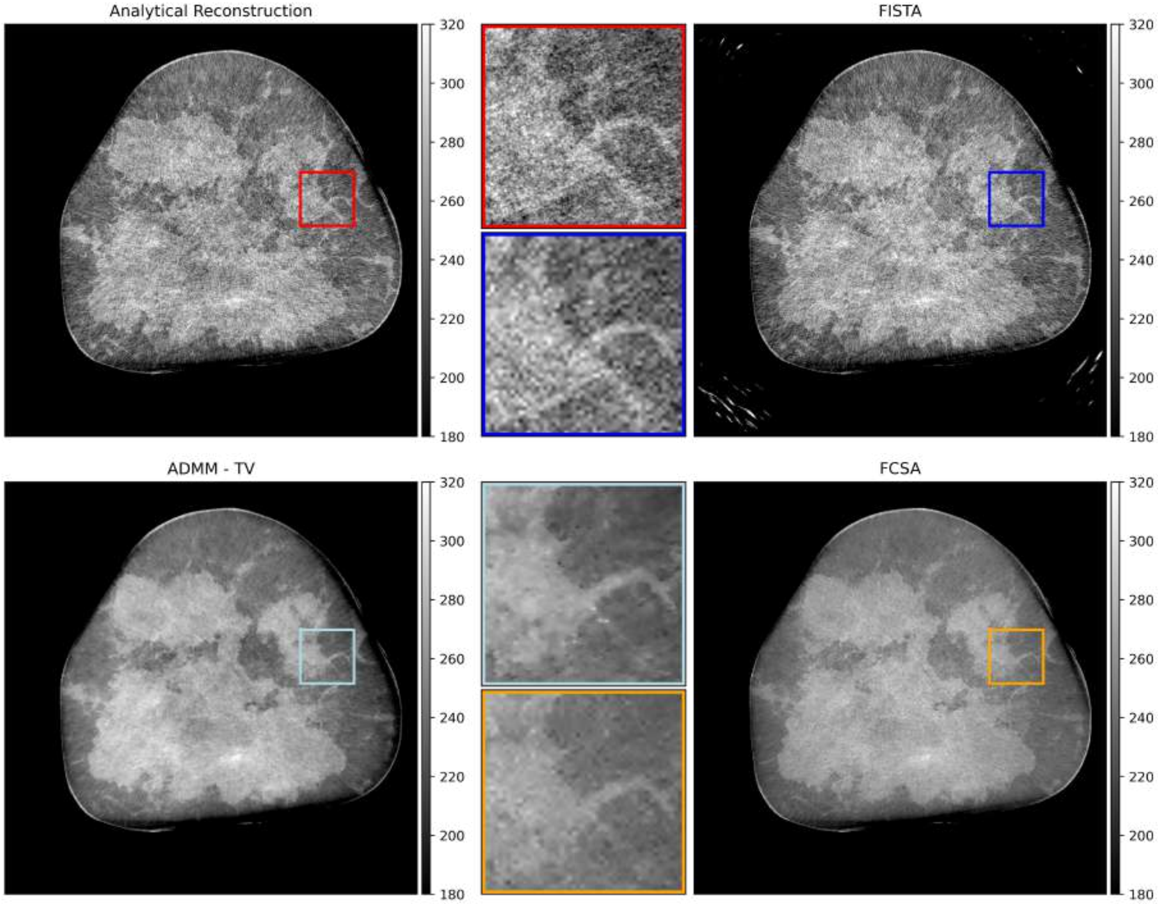

Figure 10: Reconstruction results for FBP with Hilbert filter, FISTA, TV regularization and FCSA for simulation data generated at a visibility of 0.3 and 1'000 photons/phase step. This corresponds to the high noise regime in this work.

Table 4: Quantitative evaluation of reconstruction algorithms on simulation data in the high noise regime. The best result per metric is colored in blue.

	Phantom	Analytical	ADMM-TV	FISTA	FCSA
Contrast	2.3737	2.565	3.7486	2.4729	2.0473
CNR	5.5476	1.2978	6.4972	1.7075	3.9536
SNR	63.0	16.38	66.16	23.22	82.79
MSE	0.0	419.26	502.37	388.64	306.40
SSIM	1.0	0.5199	0.5396	0.5206	0.5358

3.3 Reconstruction results for experimental data

Besides simulated data, experimental phase data was measured on a static grating interferometer with a Comet MXR-225HP/11 tungsten-anode x-ray source operated at 70kVp. The pitch size of the attenuation grating G_0, the π-shifting (at 46 keV) G_1 and the three-pieced G_2 was 4.2 μm. 1200 projections with an angular scanning interval of $2\pi/1200$ were measured with a detector of size 1314 $\times$ 128 and a detector pixel size of 150 μm. To reduce the noise level, the differential phase sinograms of 10 scans were averaged. This corresponds to $\sim$ 50 times clinical dose. Figure 7b shows the analytical reconstruction of the experimental data.

The experimental data was reconstructed with a reconstruction volume of 1314 $\times$ 1314 $\times$ 16, where the 16 slices where taken from the inner part of the breast volume between slice 21 and 37 of the original 128 slices. The reconstruction geometry is given in Table 5.

Table 5: Reconstruction geometry for experimental data.

Parameter	Value
Number of projections	1200
Angular scanning interval	$2\pi/1200$
Number of detector pixels	1314 × 16
Reconstructed image size	1314 × 1314 × 16
Sample-source distance	1.03 m
Sample-detector distance	0.753 m
Image voxel size	$86.65 \times 86.65 \times 86.65\ \mu m^3$

The algorithm-dependent hyperparameters have the same meaning as for the simulated data and were similarly determined. The specific values are summarized in Table 6.

Table 6: Algorithm-dependent reconstruction parameters for experimental data.

	Number of iterations *without* regularizer	Number of iterations *with* regularizer	Wavelet thresholds for scale (1,2,3)	Wavelet	TV weight	TV max. iteration
FISTA	-	300	(0.0001, 1, 1000)	db4	-	-
ADMM-TV	40	40	-	-	0.2	40
FCSA	-	300	(0.002, 1.5, 1000)	db4	0.05	40

Qualitative results

Figure 11 shows the qualitative comparison of FISTA and FCSA compared to an analytical reconstruction and a TV-based regularization as reference. Since the algorithms are not calibrated and a color scale normalization is not possible due to the lack of a ground truth image, the color scale limits are selected individually such that the contrast in visual inspection is good.

The FBP with a Hilbert filter achieves sharp image edges but some fine noise remains. In both FISTA and FCSA not all noise was removed and the image pixels become visible, in FISTA much more then in FCSA. The image of FCSA is smooth but the edges are slightly blurred and thin lines, as present in the magnification, start getting erased. The edges of FISTA and ADMM-TV remain sharper but thin lines also vanish. Additionally, ADDM-TV develops a salt-and-pepper noise structure overlaying the reconstruction.

Quantitative results

The best results in terms of CNR (7.7499) and SNR (83.88) are achieved by the FCSA reconstruction, while the contrast is highest in the analytically reconstructed image with 3.5537 dB. The values for contrast, CNR and SNR are summarized in Table 7 for all four reconstruction algorithms.

Table 7: Quantitative evaluation of reconstruction algorithms on experimental data in the low noise regime. The best result per metric is colored in blue.

	Analytical	ADMM-TV	FISTA	FCSA
Contrast	3.5537	3.3148	3.2621	3.1678
CNR	5.2205	4.5418	5.7010	7.7499
SNR	47.34	44.83	59.06	83.88

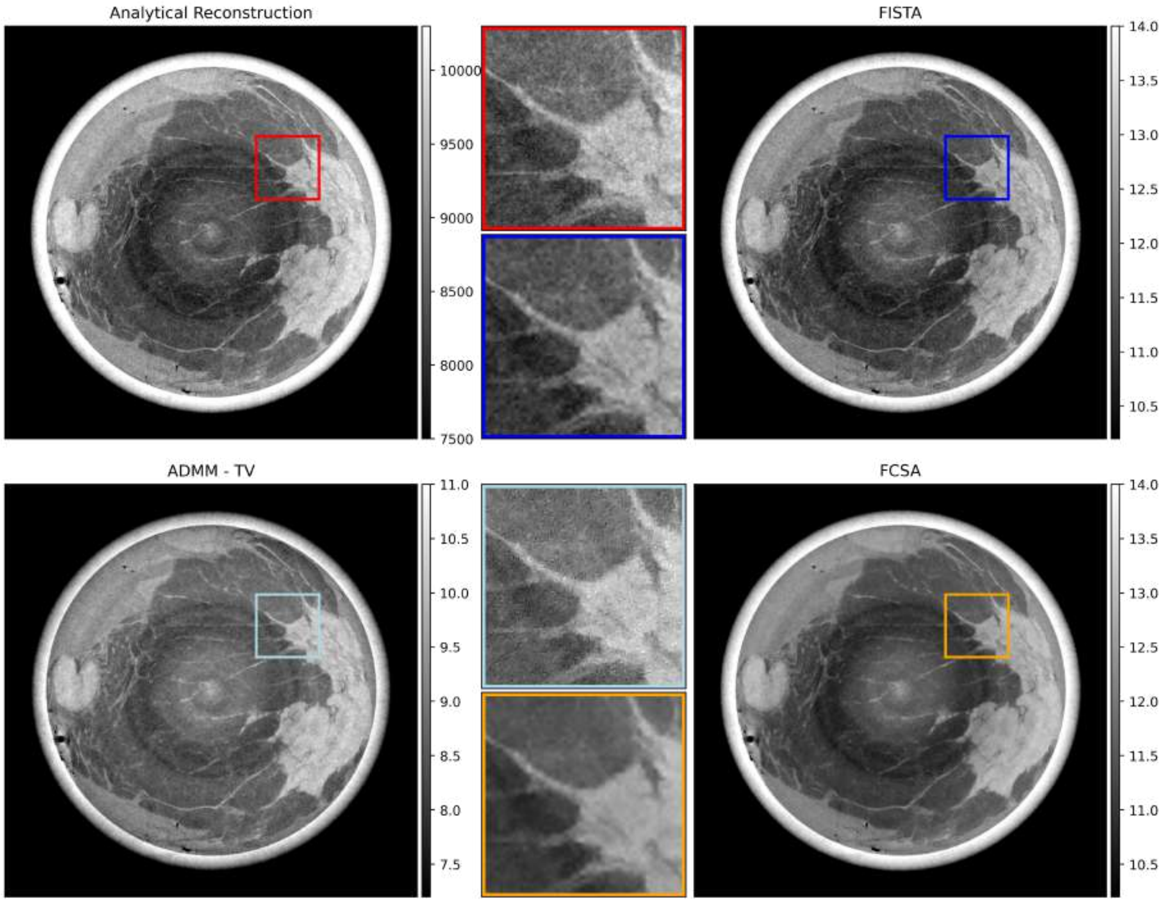

Figure 11: Reconstruction results for FBP with Hilbert filter, FISTA, ADMM-TV and FCSA for experimental data measured from a mastectomy on a static setup. The differential phase sinograms were averaged for 10 scans to reduce the noise level.

3.4 Convergence and computation time of ADMM-TV, FISTA and FCSA

As an example, the convergence of FISTA, FCSA and ADMM-TV was analysed for the simulated data at low noise level and is given in Figure 12. The steep decay of ADMM-TV at the beginning is due to the initial least-square data update without regularization of 40 iterations, whose individual normalized projection errors could not be saved.

The computational time of FISTA is the lowest with 1800 seconds including the initial computation of the Lipschitz constant that took 322 seconds. Since this computation has to be done only once for multiple measurements of the same setup geometry, the effective computation time of FISTA is 1478 seconds. The effective computation time of FCSA is 7774 seconds and ADMM-TV took 7547 seconds to finish the reconstruction.

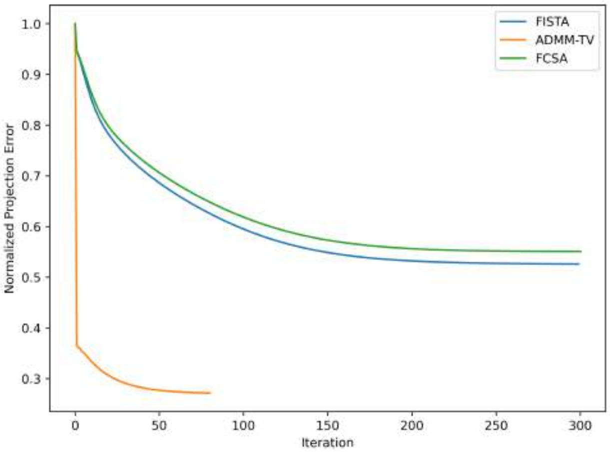

Figure 12: Convergence behaviour of FISTA, ADMM-TV and FCSA at low dose regime of simulated data.

4 Discussion

FISTA proved to be a very stable algorithm for reconstructing phase contrast GI-BCT data. Convergence is reached within 300 iterations and the computation time until convergence is the shortest of the four iterative algorithms (ISTA, FISTA, ADMM-TV and FCSA) tested in this work. However, the image quality is not as good as we had hoped. A major trade-off between noise removal and image resolution has to be made since for each lower wavelet transform scale which gets thresholded, the image resolution is reduced by up to a factor of two. Yet, the image quality might be improved with better parameter tuning. Especially the wavelet type and length as well as the wavelet thresholds have an important influence on the reconstruction output. Nevertheless, the fast iterative shrinkage thresholding algorithm can be the tool of choice when one wants to get a quick look at a set of newly measured data that can not be analytically reconstructed.

In contrast to FISTA, FCSA provides a better image quality. In the low noise regime, the image quality, both qualitatively and quantitatively, is equally good or even better than the analytically reconstructed and the ADMM-TV reference. The SNR is high and the edges still keep most of their sharpness. However, some small details can get lost. Furthermore, the contrast, and therefore the CNR, are rather reduced compared to the TV regularized reference. A contrast reducing factor might be the soft-thresholding in combination with the TV regularization. Both regularization terms reduce the amount of pixel-wise intensity, also called image energy, added per iteration step. Potentially, the combined regularization is too strong to allow a complete development of image energy, wherefore a reduced contrast results. Replacing the soft-thresholding by hard- [55] or a mixture of soft- and hard-thresholding [56] might allow better contrast development, since more image energy passes through.

Another explanation for the discrepancy in contrast values is that the ADMM-TV reconstruction might not yet have fully converged, which would also explain the high MSE of the TV solution. Since the image energy increases with each iteration step, the contrast might appear enhanced if the reconstruction has not fully converged. After all, the contrast seems increased if one tissue type has already reached its final value but the other tissue type due to its geometrical location in the image has not. A good indication for this phenomenon is the contrast and CNR value of the ground truth image, which is closer to the values of FCSA. However, a distinct source of contrast loss in FCSA or of contrast enhancement in ADMM-TV has not been identified.

A limitation of this research is that all three iterative reconstruction algorithms are not calibrated and thus the comparison of the pixel-wise intensity values is difficult. Although an intensity correction based on the ground truth image has been performed for the simulation data, the intensity values remain without defined physical unit. It is our hope that a calibration of the algorithms not only further supports the accuracy of the wavelet-based reconstruction algorithms and makes the reconstructed images physical meaningful, but also reveals further insight into the image energy and contrast composition over the iteration steps.

Nevertheless, the results on the experimental data prove the applicability and the robustness of wavelet-based shrinkage thresholding as applied in FISTA and FCSA to a certain degree. The qualitative and quantitative image analysis reveals their high performance in contrast, CNR and SNR almost outrunning the analytical reconstruction method. Especially FCSA has achieved a convincing image quality that is better than the two references. Yet, the dose is due to the 10 scan averaging much higher than clinical regulations would allow, which means that the noise level in general is much lower than we would observe in a clinical setting.

Although the high noise level simulation coincides with the statistics of a measurement taken at multiple times the maximal clinical dose, the image quality in this regime is for all four algorithms not near the requirements for clinical use. FISTA has difficulties in tackling the noise, yet the edges of tissue boundaries stay sharp and the contrast is still apparent. In FCSA the SNR is high, yet the edges in the image become blurred and a lot of details get lost due to low contrast. A reason for the poor performance of both algorithms is the noise nature of phase. Not only has the retrieved phase signal much more noise but noise at the lower end of the frequency spectrum. Besides those two algorithms, ADMM-TV also has a low performance in image quality. As to our knowledge, so far no iterative reconstruction algorithm with hand-crafted priors has achieved satisfactory results with a clinically compatible dose. The best performance in iterative phase reconstruction for GI-BCT in our group has been achieved with a machine learning-based (ML-based) regularization but has no yet been published.

The performance of ADMM-TV, FISTA and especially of FCSA might improve by adding automated or ML-based hyperparameter tuning. FCSA has more than eight hyperparameters which have to be determined including the thresholding method, the total iteration number, the wavelet, the DWT scale, the thresholds per scale, the TV weight parameter, the TV maximal iteration number as well as the wavelet and TV weights for the regularized image averaging. Due to this immense number and time limitations, we decided to combine literature-based hyperparameters, such as soft-thresholding, [25, 26], the Daubechies wavelet [38, 39, 40], the DWT scale of 3 [39, 56] and the averaging weight of 0.5 [45], with manual grid search on the total iteration number, the wavelet thresholds and the TV parameters.

Despite the fact that the wavelet transform and the soft-thresholding are done slice-wise, their computational expenses are not immense. The limiting step in FCSA is the Chambolle TV estimator as it is an iterative estimator. Consequently, the computation time of FCSA is much higher than that of FISTA. However, when comparing the computation time to the ADMM-TV algorithm, they are of similar range although FCSA has performed more iterations and TV estimations. Therefore, it is evident that FCSA's data update term is computationally less expensive. This also leads to the conclusion that for bigger datasets or datasets where more iterations are needed to reach convergence, FCSA will overtake ADMM-TV in terms of computation time.

So far, all wavelet regularization has been applied in plane in x-y-direction. A next step could be to add wavelet regularization in 3D, which would also take the off-plane z-axis into account. Moreover, wavelet denoising could also be considered in the sinogram domain prior to reconstruction. The less noise is fed into the reconstruction algorithms, the better their performace will be. Further work should also include iterative phase reconstruction with shearlet as well as shearlet-wavelet-combined regularization. Shearlets are better in filtering structural noise which is aligned in non-horizontal, -vertical and -diagonal direction. Since noise in phase contrast often appears as a radial pattern originating from the rotation axis, many such noise patterns disturb the reconstructed image without a regularization term [57, 58].

The results of this project build a solid foundation for an intensity-based iterative reconstruction algorithm with only wavelet- or wavelet-TV-based regularization at least in low noise regime, which should be targeted in further research. The developed wavelet regularization and reconstruction code can be used to implement such a method, though the forward operator must be adjusted and will not be linear anymore. Additionally, the inverse problem will lose its convexity and FISTA resp. FCSA might not converge.

5 Conclusion

The scope of this project was to try hand-crafted wavelet-based regularization for phase reconstruction of grating interferometry breast computed tomography. A fast iterative shrinkage thresholding algorithm with a three-scaled wavelet transform and applied soft-thresholding was implemented. The algorithm proved to be computationally efficient and stable for ill-posed but convex linear inverse problems as it is the case for differential phase contrast reconstruction. However, the image quality has not been convincing, since a lot of noise remains in the reconstruction and a large resolution drop occurs if too much thresholding is performed, especially on lower wavelet transform scales. Although better hyperparameter tuning might lead to improved reconstruction results, the observation of the FISTA results lead to the conclusion that wavelet-based regularization might not be powerful enough to deal with the unique composition of noise in phase.

As an addition, a combined wavelet-TV regularization was implemented in form of the fast composite splitting algorithm. The FCSA has produced good image quality in the low noise regime for both simulated and experimental data. The quantitative and qualitative comparison to an analytical and a TV regularized iterative reconstruction led to the conclusion that the algorithm has the potential to outperform both references but a more evolved hyperparameter tuning is needed. More than eight hyperparameters are available. Due to time reasons only for four of them a manual grid search was completed. The other parameters were set based on literature standards.

FCSA has a drawback in computation time. The TV estimation is computationally expensive and leads to a long reconstruction time. Yet, the reconstruction time is comparable to a standard iterative algorithm with TV regularizer. An important point to mention is the great decrease in image quality for higher noise levels. Despite the fact that the visibility was simulated to be much higher than what is achievable with current gratings and that the dose is quite above the clinical limit, all tested algorithms struggle with the strong noise. A further step towards clinical dose is the use of intensity-based reconstruction instead of phase stepping which will reduce the dose by factor five. Even then, to reach an operation point for clinical usage, a lot of improvements in grating fabrication, reconstruction algorithms and denoising methods will be needed.

Combined wavelet-TV regularization has the potential to be a valuable tool in iterative phase reconstruction. By including an automated or machine learning-based hyperparameter tuning, the reconstruction quality will likely further rise. Additionally, the introduction of shearlet-based regularization to GI-BCT phase reconstruction should be considered.

References

[1] H. Sung, J. Ferlay, R. L. Siegel, M. Laversanne, I. Soerjomataram, A. Jemal, and F. Bray, “Global cancer statistics 2020: Globocan estimates of incidence and mortality worldwide for 36 cancers in 185 countries,” *CA: a cancer journal for clinicians*, vol. 71, no. 3, pp. 209–249, 2021.

[2] M. G. Marmot, D. Altman, D. Cameron, J. Dewar, S. Thompson, and M. Wilcox, “The benefits and harms of breast cancer screening: an independent review,” *British journal of cancer*, vol. 108, no. 11, pp. 2205–2240, 2013.

[3] C. D. Lehman, R. F. Arao, B. L. Sprague, J. M. Lee, D. S. Buist, K. Kerlikowske, L. M. Henderson, T. Onega, A. N. Tosteson, G. H. Rauscher *et al.*, “National performance benchmarks for modern screening digital mammography: update from the breast cancer surveillance consortium,” *Radiology*, vol. 283, no. 1, pp. 49–58, 2017.

[4] S. J. Magny, R. Shikhman, and A. L. Keppke, “Breast imaging reporting and data system,” in *StatPearls [Internet]*. StatPearls publishing, 2021.

[5] S.-A. Zhou and A. Brahme, “Development of phase-contrast x-ray imaging techniques and potential medical applications,” *Physica Medica*, vol. 24, no. 3, pp. 129–148, 2008.

[6] S. Wilkins, Y. I. Nesterets, T. Gureyev, S. Mayo, A. Pogany, and A. Stevenson, “On the evolution and relative merits of hard x-ray phase-contrast imaging methods,” *Philosophical Transactions of the Royal Society A: Mathematical, Physical and Engineering Sciences*, vol. 372, no. 2010, p. 20130021, 2014.

[7] R. Fitzgerald, “Phase-sensitive x-ray imaging; new approaches that can detect x-ray phase shifts within soft tissues show promise for clinical and biological applications,” *Physics today*, vol. 53, pp. 23–28, 2000.

[8] T. J. Davis, D. Gao, T. Gureyev, A. Stevenson, and S. Wilkins, “Phase-contrast imaging of weakly absorbing materials using hard x-rays,” *Nature*, vol. 373, no. 6515, pp. 595–598, 1995.

[9] J. Miao, R. L. Sandberg, and C. Song, “Coherent x-ray diffraction imaging,” *IEEE Journal of selected topics in quantum electronics*, vol. 18, no. 1, pp. 399–410, 2011.

[10] M. Stampanoni, R. Mokso, F. Marone, J. Vila-Comamala, S. Gorelick, P. Trtik, K. Jefimovs, and C. David, “Phase-contrast tomography at the nanoscale using hard x rays,” *Physical Review B*, vol. 81, no. 14, p. 140105, 2010.

[11] A. Groso, R. Abela, and M. Stampanoni, “Implementation of a fast method for high resolution phase contrast tomography,” *Optics express*, vol. 14, no. 18, pp. 8103–8110, 2006.

[12] F. Pfeiffer, T. Weitkamp, O. Bunk, and C. David, “Phase retrieval and differential phase-contrast imaging with low-brilliance x-ray sources,” *Nature physics*, vol. 2, no. 4, pp. 258–261, 2006.

[13] Z. Wang and B. Han, “Advanced iterative algorithm for phase extraction of randomly phase-shifted interferograms,” *Optics letters*, vol. 29, no. 14, pp. 1671–1673, 2004.

[14] K. Hashimoto, H. Takano, and A. Momose, “Improved reconstruction method for phase stepping data with stepping errors and dose fluctuations,” *Optics Express*, vol. 28, no. 11, pp. 16 363–16 384, 2020.

[15] L. Birnbacher, M. Viermetz, W. Noichl, S. Allner, A. Fehringer, M. Marschner, M. von Teuffenbach, M. Willner, K. Achterhold, P. B. Noël *et al.*, “Tilted grating phase-contrast computed tomography using statistical iterative reconstruction,” *Scientific Reports*, vol. 8, no. 1, pp. 1–8, 2018.

[16] I. Bukreeva, V. Asadchikov, A. Buzmakov, M. Chukalina, A. Ingacheva, F. Palermo, M. Fratini, and A. Cedola, “Simultaneous iterative reconstruction method for high resolution x-ray phase-contrast tomography,” in *Twelfth International Conference on Machine Vision (ICMV 2019)*, vol. 11433. International Society for Optics and Photonics, 2020, p. 114331V.

[17] G. Ju, X. Qi, H. Ma, and C. Yan, "Feature-based phase retrieval wavefront sensing approach using machine learning," *Optics express*, vol. 26, no. 24, pp. 31 767–31 783, 2018.

[18] P. Zhu, K. Zhang, Z. Wang, Y. Liu, X. Liu, Z. Wu, S. A. McDonald, F. Marone, and M. Stampanoni, "Low-dose, simple, and fast grating-based x-ray phase-contrast imaging," *Proceedings of the National Academy of Sciences*, vol. 107, no. 31, pp. 13 576–13 581, 2010.

[19] R. Raupach and T. G. Flohr, "Analytical evaluation of the signal and noise propagation in x-ray differential phase-contrast computed tomography," *Physics in Medicine & Biology*, vol. 56, no. 7, p. 2219, 2011.

[20] J. Xu, Z. Wang, S. van Gogh, M. Rawlik, S. Spindler, and M. Stampanoni, "Intensity-based iterative reconstruction for helical grating interferometry breast ct with static grating configuration," *Optics Express*, vol. 30, no. 8, pp. 13 847–13 863, 2022.

[21] M. v. Teuffenbach, T. Koehler, A. Fehringer, M. Viermetz, B. Brendel, J. Herzen, R. Proksa, E. J. Rummeny, F. Pfeiffer, and P. B. Noël, "Grating-based phase-contrast and dark-field computed tomography: a single-shot method," *Scientific reports*, vol. 7, no. 1, pp. 1–8, 2017.

[22] M. Guerquin-Kern, D. Van De Ville, C. Vonesch, J.-C. Baritaux, K. P. Pruessmann, and M. Unser, "Wavelet-regularized reconstruction for rapid mri," in *2009 IEEE International Symposium on Biomedical Imaging: From Nano to Macro.* IEEE, 2009, pp. 193–196.

[23] M. Guerquin-Kern, M. Haberlin, K. P. Pruessmann, and M. Unser, "A fast wavelet-based reconstruction method for magnetic resonance imaging," *IEEE transactions on medical imaging*, vol. 30, no. 9, pp. 1649–1660, 2011.

[24] M. Islam, R. Islam *et al.*, "Multiscale wavelet-based regularized reconstruction algorithm for three-dimensional compressed sensing magnetic resonance imaging," *Signal, Image and Video Processing*, vol. 15, no. 7, pp. 1487–1495, 2021.

[25] I. Daubechies, M. Defrise, and C. De Mol, "An iterative thresholding algorithm for linear inverse problems with a sparsity constraint," *Communications on Pure and Applied Mathematics: A Journal Issued by the Courant Institute of Mathematical Sciences*, vol. 57, no. 11, pp. 1413–1457, 2004.

[26] A. Beck and M. Teboulle, "A fast iterative shrinkage-thresholding algorithm for linear inverse problems," *SIAM journal on imaging sciences*, vol. 2, no. 1, pp. 183–202, 2009.

[27] C. Kottler, F. Pfeiffer, O. Bunk, C. Grünzweig, and C. David, "Grating interferometer based scanning setup for hard x-ray phase contrast imaging," *Review of Scientific Instruments*, vol. 78, no. 4, p. 043710, 2007.

[28] G. Stoilov and T. Dragostinov, "Phase-stepping interferometry: five-frame algorithm with an arbitrary step," *Optics and Lasers in Engineering*, vol. 28, no. 1, pp. 61–69, 1997.

[29] A. W. Lohmann and D. Silva, "An interferometer based on the talbot effect," *Optics Communications*, vol. 2, no. 9, pp. 413–415, 1971.

[30] T. Weitkamp, A. Diaz, C. David, F. Pfeiffer, M. Stampanoni, P. Cloetens, and E. Ziegler, "X-ray phase imaging with a grating interferometer," *Optics express*, vol. 13, no. 16, pp. 6296–6304, 2005.

[31] A. Momose, "Recent advances in x-ray phase imaging," *Japanese journal of applied physics*, vol. 44, no. 9R, p. 6355, 2005.

[32] J. Fu, S. Schleede, R. Tan, L. Chen, M. Bech, K. Achterhold, M. Gifford, R. Loewen, R. Ruth, and F. Pfeiffer, "An algebraic iterative reconstruction technique for differential x-ray phase-contrast computed tomography," *Zeitschrift für Medizinische Physik*, vol. 23, no. 3, pp. 186–193, 2013.

[33] D. Zhang, "Wavelet transform," in *Fundamentals of Image Data Mining.* Springer, 2019, pp. 35–44.

[34] J. Kovacevic and W. Sweldens, “Wavelet families of increasing order in arbitrary dimensions,” *IEEE Transactions on Image Processing*, vol. 9, no. 3, pp. 480–496, 2000.

[35] D. Ravichandran, R. Nimmatoori, and M. Gulam Ahamad, “Mathematical representations of 1d, 2d and 3d wavelet transform for image coding,” *Int. J. Adv. Comput. Theory Eng*, vol. 5, pp. 1–8, 2016.

[36] V. R. Algazi, G. E. Ford, and H. Chen, “Linear filtering of images based on properties of vision,” *IEEE transactions on image processing*, vol. 4, no. 10, pp. 1460–1464, 1995.

[37] C. Vonesch, T. Blu, and M. Unser, “Generalized daubechies wavelet families,” *IEEE Transactions on Signal Processing*, vol. 55, no. 9, pp. 4415–4429, 2007.

[38] J. Ma and M. März, “A multilevel based reweighting algorithm with joint regularizers for sparse recovery,” *arXiv preprint arXiv:1604.06941*, 2016.

[39] N. Terzija and H. McCann, “Wavelet-based image reconstruction for hard-field tomography with severely limited data,” *IEEE Sensors Journal*, vol. 11, no. 9, pp. 1885–1893, 2010.

[40] Q. Xu, A. Sawatzky, M. A. Anastasio, and C. O. Schirra, “Sparsity-regularized image reconstruction of decomposed k-edge data in spectral ct,” *Physics in Medicine & Biology*, vol. 59, no. 10, p. N65, 2014.

[41] G. Lee, R. Gommers, F. Waselewski, K. Wohlfahrt, and A. O’Leary, “Pywavelets: A python package for wavelet analysis,” *Journal of Open Source Software*, vol. 4, no. 36, p. 1237, 2019.

[42] I. Loris and C. Verhoeven, “On a generalization of the iterative soft-thresholding algorithm for the case of non-separable penalty,” *Inverse Problems*, vol. 27, no. 12, p. 125007, 2011.

[43] D. L. Donoho, “De-noising by soft-thresholding,” *IEEE transactions on information theory*, vol. 41, no. 3, pp. 613–627, 1995.

[44] M. T. Chu and J. L. Watterson, “On a multivariate eigenvalue problem, part i: Algebraic theory and a power method,” *SIAM Journal on scientific computing*, vol. 14, no. 5, pp. 1089–1106, 1993.

[45] J. Huang, S. Zhang, and D. Metaxas, “Efficient mr image reconstruction for compressed mr imaging,” *Medical Image Analysis*, vol. 15, no. 5, pp. 670–679, 2011.

[46] L. I. Rudin, S. Osher, and E. Fatemi, “Nonlinear total variation based noise removal algorithms,” *Physica D: nonlinear phenomena*, vol. 60, no. 1-4, pp. 259–268, 1992.

[47] P. Li, W. Chen, and M. K. Ng, “Compressive total variation for image reconstruction and restoration,” *Computers & Mathematics with Applications*, vol. 80, no. 5, pp. 874–893, 2020.

[48] A. Chambolle, “An algorithm for total variation minimization and applications,” *Journal of Mathematical imaging and vision*, vol. 20, no. 1, pp. 89–97, 2004.

[49] F. Pfeiffer, C. Kottler, O. Bunk, and C. David, “Hard x-ray phase tomography with low-brilliance sources,” *Physical review letters*, vol. 98, no. 10, p. 108105, 2007.

[50] S. Boyd, N. Parikh, E. Chu, B. Peleato, J. Eckstein *et al.*, “Distributed optimization and statistical learning via the alternating direction method of multipliers,” *Foundations and Trends® in Machine learning*, vol. 3, no. 1, pp. 1–122, 2011.

[51] P. Virtanen, R. Gommers, T. E. Oliphant, M. Haberland, T. Reddy, D. Cournapeau, E. Burovski, P. Peterson, W. Weckesser, J. Bright *et al.*, “Scipy 1.0: fundamental algorithms for scientific computing in python,” *Nature methods*, vol. 17, no. 3, pp. 261–272, 2020.

[52] S. van Gogh, Z. Wang, M. Rawlik, C. Etmann, S. Mukherjee, C.-B. Schönlieb, F. Angst, A. Boss, and M. Stampanoni, “Insidenet: Interpretable nonexpansive data-efficient network for denoising in grating interferometry breast ct,” *Medical physics*, 2022.

[53] S. Shim, N. Saltybaeva, N. Berger, M. Marcon, H. Alkadhi, and A. Boss, "Lesion detectability and radiation dose in spiral breast ct with photon-counting detector technology: a phantom study," *Investigative Radiology*, vol. 55, no. 8, pp. 515–523, 2020.

[54] W. Van Aarle, W. J. Palenstijn, J. De Beenhouwer, T. Altantzis, S. Bals, K. J. Batenburg, and J. Sijbers, "The astra toolbox: A platform for advanced algorithm development in electron tomography," *Ultramicroscopy*, vol. 157, pp. 35–47, 2015.

[55] J. B. Weaver, Y. Xu, D. Healy Jr, and L. Cromwell, "Filtering noise from images with wavelet transforms," *Magnetic Resonance in Medicine*, vol. 21, no. 2, pp. 288–295, 1991.

[56] C. Peng, B. Qiu, M. Li, Y. Yang, C. Zhang, L. Gong, and J. Zheng, "Gpu-accelerated dynamic wavelet thresholding algorithm for x-ray ct metal artifact reduction," *IEEE Transactions on Radiation and Plasma Medical Sciences*, vol. 2, no. 1, pp. 17–26, 2017.

[57] B. Vandeghinste, B. Goossens, R. Van Holen, C. Vanhove, A. Pižurica, S. Vandenberghe, and S. Staelens, "Iterative ct reconstruction using shearlet-based regularization," *IEEE Transactions on Nuclear Science*, vol. 60, no. 5, pp. 3305–3317, 2013.

[58] X. Shao, C. Wei, Y. Xie, Z. Wang, and Y. Shen, "Shearlet-based compressed sensing with non-local similarity for mri breast image reconstruction," *IET Signal Processing*, vol. 15, no. 9, pp. 573–583, 2021.

Eidgenössische Technische Hochschule Zürich
Swiss Federal Institute of Technology Zurich

Declaration of originality

The signed declaration of originality is a component of every semester paper, Bachelor's thesis, Master's thesis and any other degree paper undertaken during the course of studies, including the respective electronic versions.

Lecturers may also require a declaration of originality for other written papers compiled for their courses.

I hereby confirm that I am the sole author of the written work here enclosed and that I have compiled it in my own words. Parts excepted are corrections of form and content by the supervisor.

Title of work (in block letters):

Wavelet-based regularizers for iterative tomographic reconstruction in Grating Interferometry Breast CT

Authored by (in block letters):

For papers written by groups the names of all authors are required.

Name(s):	**First name(s):**
Haltmeier	Sandra

With my signature I confirm that
- I have committed none of the forms of plagiarism described in the 'Citation etiquette' information sheet.
- I have documented all methods, data and processes truthfully.
- I have not manipulated any data.
- I have mentioned all persons who were significant facilitators of the work.

I am aware that the work may be screened electronically for plagiarism.

Place, date

Villigen, 07.06.2022

Signature(s)

For papers written by groups the names of all authors are required. Their signatures collectively guarantee the entire content of the written paper.